Tunable Interaction-Induced Localization of Surface Electrons in Antidot Nanostructured Bi_2Te_3 Thin Films

Hong-Chao Liu,[†,#] Hai-Zhou Lu,[‡,#] Hong-Tao He,[†,§] Baikui Li,[†] Shi-Guang Liu,[†] Qing Lin He,[†] Gan Wang,[†,§] Iam Keong Sou,[†] Shun-Qing Shen,[‡,*] and Jiannong Wang[†,*]

[†]Department of Physics, The Hong Kong University of Science and Technology, Clear Water Bay, Hong Kong, China, [‡]Department of Physics, The University of Hong Kong, Pokfulam Road, Hong Kong, China, and [§]Department of Physics, South University of Science and Technology of China, Shenzhen, Guangdong 518055, China. [#]H.-C. Liu and H.-Z. Lu contributed equally to this work.

ABSTRACT Recently, a logarithmic decrease of conductivity has been observed in topological insulators at low temperatures, implying a tendency of localization of surface electrons. Here, we report quantum transport experiments on the topological insulator Bi_2Te_3 thin films with arrayed antidot nanostructures. With increasing density of the antidots, a systematic decrease is observed in the slope of the logarithmic temperature-dependent conductivity curves, indicating the electron–electron interaction can be tuned by the antidots. Meanwhile, the weak antilocalization effect revealed in magnetoconductivity exhibits an enhanced dominance of electron–electron interaction among decoherence mechanisms. The observation can be understood from an antidot-induced reduction of the effective dielectric constant, which controls the interactions between the surface electrons. Our results clarify the indispensable role of the electron–electron interaction in the localization of surface electrons and indicate the localization of surface electrons in an interacting topological insulator.

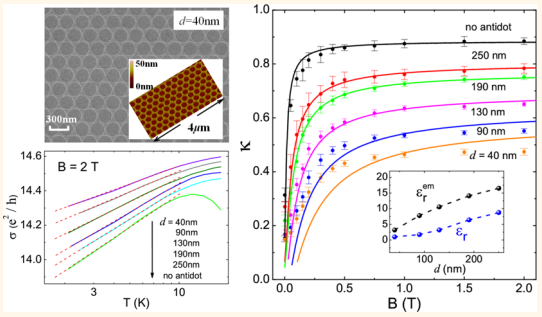

KEYWORDS: topological insulator · surface states · antidot · electron–electron interaction · weak antilocalization effect

Topological insulators are gapped band insulators, but have gapless modes on their boundaries.[1−4] Recently, there is growing interest in many-body interactions in topological states of matter.[5−13] Despite the tremendous interest in physics driven by strong interaction, in the prototype materials of topological insulators, such as Bi_2Se_3 and Bi_2Te_3,[14−16] the interaction is thought to be fairly weak due to the large background lattice dielectric constant.[10,13] Nevertheless, an interaction-induced transport phenomenon resulting from the interplay of interaction and disorder may occur even for weak interactions as long as disorder scattering is sufficiently strong.[17−19] In a two-dimensional (2D) electron gas, the effect manifests itself as a decrease in conductivity with logarithmically decreasing temperature. In particular, in sufficiently strong magnetic fields, the effect could be identified when other effects such as weak localization (WL) or weak antilocalization (WAL), which may also exhibit logarithmic temperature dependence,[19] are suppressed. The signature of the interaction effect has been observed in recent transport experiments on Bi_2Se_3 and Bi_2Te_3,[20−25] but convincing quantitative comparison is still lacking.[26] A direct way to verify the effect is to modulate the interaction between the surface electrons, then to measure the responses of the finite-temperature conductivity and magnetoconductivity. However, the modulation of interactions between electrons in a solid is difficult, thus was rarely addressed.

In this article, we report quantum transport experiments by introducing antidot nanostructures in topological insulators. In finite-temperature conductivity measurements, as the antidot density changes, we observe a continuous and repeatable change in the slope of the conductivity as a function of logarithmic temperature, indicating that the denser antidots suppress the tendency of localization of the surface electrons. Meanwhile, the WAL effect manifested in the magnetoconductivity

* Address correspondence to sshen@hku.hk; phjwang@ust.hk.

Received for review July 21, 2014 and accepted September 3, 2014.

Published online September 03, 2014
10.1021/nn504014e

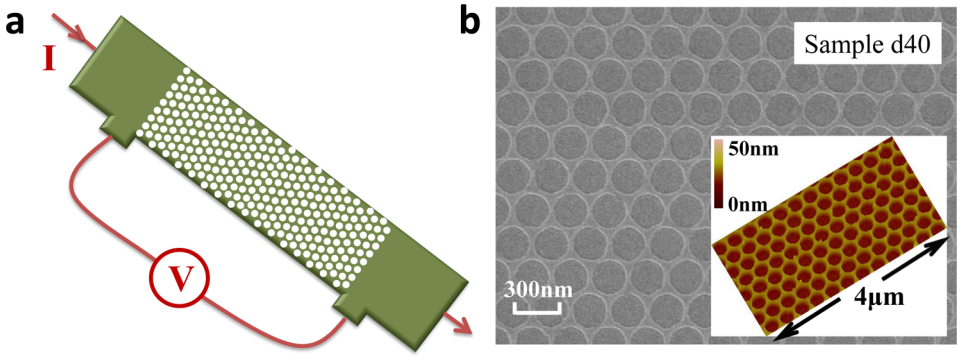

Figure 1. (a) Schematic illustration of a Hall bar sample with antidot array. (b) Scanning electron microscopy image of a Bi_2Te_3 thin film with antidot array, where the edge-to-edge distance between antidots is d = 40 nm. The inset is its atomic force microscopy image, indicating the antidots' depths (~25 nm) are larger than the Bi_2Te_3 film thickness (20 nm).

measurements also shows a tunable localization tendency with the antidot density. It is well accepted that the Dirac fermions cannot be localized by impurities and disorders, while the ordinary electrons can be easily localized in two dimensions. Our experimental data could not be understood within the framework of the existing theories. In order to explain our experimental observations, the electron−electron interaction must inevitably be taken into account. We propose a modulation mechanism wherein antidot array induces a change in the effective dielectric constant of the system, which in turn modulates the electron−electron interaction. The experimental data are fitted reasonably well when this modulation mechanism is included in the transport theory for interacting and disordered Dirac fermions.[27] We therefore show the indispensable role of the interaction in localization of the surface electrons in disordered topological insulators.

RESULTS AND DISCUSSION

The thickness of the Bi_2Te_3 thin film used in the experiment is 20 nm. A series of antidots arrayed in a periodic triangular lattice are fabricated between the voltage-measuring probes of the samples, as shown in Figure 1a. For five different nanostructured samples in our experiment, the edge-to-edge distances d of two neighboring antidots are 40, 90, 130, 190, and 250 nm, respectively. A smaller value of d represents a larger density of antidots. The diameter of each antidot is fixed at 200 nm for all samples. Figure 1b and its inset show the scanning electron microscopy (SEM) and atomic force microscopy (AFM) images, respectively, of the antidot nanostructured Bi_2Te_3 film with d = 40 nm (sample d40).

Low-temperature dependence of conductivity can reveal the tendency of localization or delocalization at low temperatures. Figure 2a shows the logarithmic temperature-dependent conductivity $\sigma(T)$ curves of different antidot nanostructured samples and a no-antidot thin film sample as a reference, in the absence of a magnetic field. All curves are normalized by their

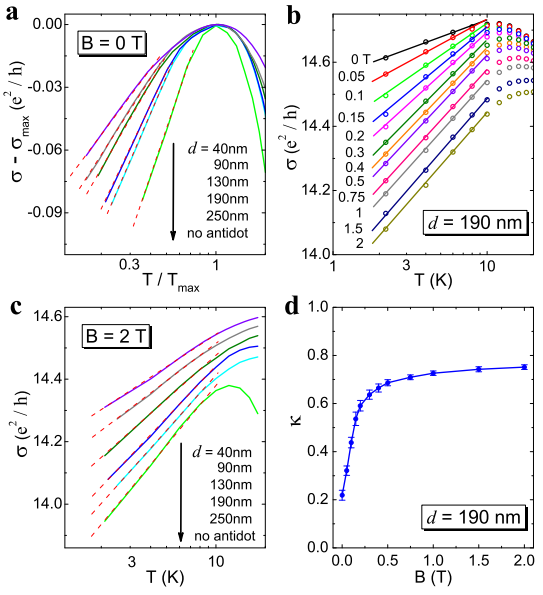

Figure 2. (a) Measured logarithmic temperature-dependent conductivity (solid lines) at zero magnetic field for all samples with the edge-to-edge distance between antidots d indicated. The red dashed lines are a guide for the eye. (b) Measured logarithmic temperature-dependent conductivity at indicated perpendicular magnetic fields (open circles) for sample d190. Solid lines are the linear fitting curves. (c) Measured temperature-dependent conductivity (solid lines) at B = 2 T for all samples with d indicated. The curves are offset for clarity, and the red dashed lines are a guide for the eye. (d) Slope obtained by linear fitting the curves in (b) plotted (solid symbols) as a function of magnetic field for sample d190. Solid lines are a guide for the eye.

maximum conductivities and corresponding temperatures. Below a threshold temperature (typically ~10 K), it is evident that for all samples $\sigma(T)$ decreases linearly with decreasing ln$T$, manifesting the localization tendency. This means that all electrons in both bulk and surface states tend to be localized and the samples become insulating with decreasing temperature. In Figure 2a, the linear slopes of $\sigma(T)$ curves decrease monotonically as the antidot separation d decreases, indicating the antidot array creates a continuous and systematic change in the localization tendency. A magnetic field applied perpendicular to the sample

surface is found to strengthen the localization tendency. Taking sample d190 as an example, Figure 2b shows a series of $\sigma(T)$ curves at different magnetic fields ranging from 0 to 2 T. With increasing magnetic field, the conductivity shifts downward and the slopes of the $\sigma(T)$ curves become steeper. The slope can be defined qualitatively as $\kappa = (\pi h/e^2)(\partial\sigma/\partial \ln T)$: A steeper slope or a larger κ means an enhanced localization tendency. By linear fitting the curves in Figure 2b, the obtained κ are plotted in Figure 2d as a function of magnetic field B. A sharp increase of the slope at low magnetic fields ($B < 0.5$ T) and almost constant slope when $B > 0.5$ T are observed, which indicates that the localization tendency of electrons is strengthened by the applied magnetic field. All samples show a similar dependence of the slope on applied magnetic field, which will be analyzed in details later in Figure 4b. Figure 2c shows $\sigma(T)$ curves of all samples with $B = 2$ T. As it can be seen, the dependence of the slope on the antidot array density is the same as the case with $B = 0$ T; that is, the linear slopes of $\sigma(T)$ curves decrease monotonically as the antidot density increases.

In order to understand the sharp increase of the slope in low-field regions in Figure 2b and d, the magnetoconductivity has been measured for all samples and is shown in Figure 3a. As it can be seen, magnetoconductivity, which is defined as $\delta\sigma(B) = \sigma(B) - \sigma(B = 0)$, is negative and exhibits a cusp around $B = 0$ T for all samples at 2.1 K, which is a typical signature of the WAL effect as a result of the π Berry phase for the surface electrons in topological insulators.[28−37] It is known that the WAL effect enhances the conductivity with decreasing temperature and follows a ln$T$ dependence in two dimensions,[19] so it gives a negative contribution to the slope observed in $\sigma(T)$ curves. However, the WAL effect can be quenched by applying a small magnetic field, as shown by the negative magnetoconductivity in Figure 3a. As a result, the quenching of the WAL effect leads to the sharp increase of the slope of the $\sigma(T)$ curves as well as the downshift of $\sigma(T)$ curves in the low-field region, as shown in Figure 2b and d. On the other hand, the negative magnetoconductivity is suppressed with decreasing antidot separation d as shown in Figure 3a. Using the magnetoconductivity formula for interacting Dirac fermions,[27,38] the measured magnetoconductivity curves in Figure 3a can be quantitatively analyzed. The phase coherence length ℓ_ϕ can be obtained by the fittings and is shown in Figure 3b as a function of d. We note that the phase coherence length is shortened with decreasing d, indicating that denser antidot array tends to enhance the inelastic scattering, which breaks the phase coherence and gives rise to the suppression of the magnetoconductivity in Figure 3a.

Figure 3c shows the magnetoconductivity of sample d190 measured at temperatures from 2.1 to 12 K. By fitting the magnetoconductivity curve at each

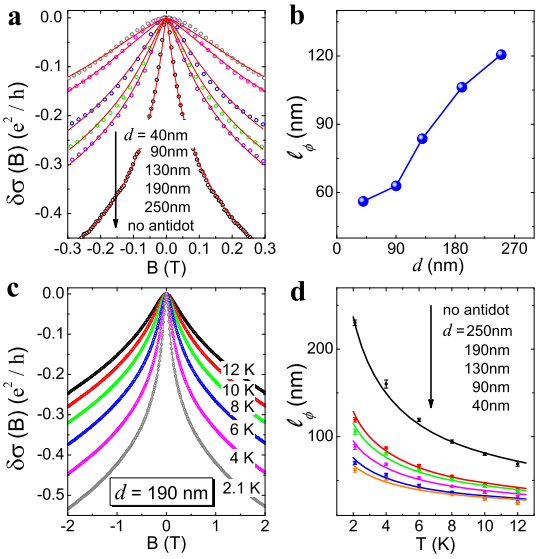

Figure 3. (a) Measured (open symbols) and fitted (solid curves) magnetoconductivity curves of all samples at 2.1 K with the magnetic field B perpendicular to the sample surface. (b) ℓ_ϕ as a function of d obtained by fitting the magnetoconductivity curves in (a).[27,38] (c) Measured magnetoconductivity curves of sample d190 at different temperatures. (d) The phase coherence length ℓ_ϕ *vs* temperature T. Solid symbols are obtained by fitting magnetoconductivity curves at different temperatures for all samples. Solid curves are the fittings to the solid symbols with $\ell_\phi \propto T^{-p/2}$, and the fitted exponents $p/2$ are given in Table 1.

temperature, the ℓ_ϕ dependence on T can be obtained. The relationship between ℓ_ϕ and T for all the samples is plotted in Figure 3d. Empirically, ℓ_ϕ increases with decreasing temperature according to $\ell_\phi \propto T^{-p/2}$, where the exponent p is positive.[39] Fitting the data shown in Figure 3d, the obtained exponents $p/2$ for all samples are given in Table 1. In a 2D disordered metal, if the dominant decoherence mechanism is the electron−electron interaction, then $p = 1$, or the electron−phonon interaction, then $p = 3$.[19] In our case, the exponent p is close to 1 for all samples and approaches 1 as the antidot density increases, which provides strong and explicit evidence that the decoherence due to electron−electron interaction is dominant and enhanced by antidot array.

To summarize our experimental measurements, (i) $\sigma(T)$ decreases linearly with the logarithmic temperature, indicating the localization tendency of surface electrons. (ii) The slope κ of $\sigma(T)$ *vs* ln$T$ curves decreases when the separation of the antidots decreases; that is, the density of antidots increases. The denser the antidot array, the weaker the localization tendency of surface electrons. (iii) The magnetoconductivity reveals the WAL effect from surface electrons. The fitting exponent p in the temperature-dependent phase coherent length is close to 1, indicating that the electron−electron interaction is the dominant decoherence mechanism.

These observations cannot be simply understood within the framework of the localization theory. It is

TABLE 1. Obtained Parameters for All Samples[38a]

	ℓ (nm)	ℓ_ϕ (nm)	$p/2$	ε_r	ε_r^{em}
no antidot	20.0	230.2 ± 3.1	0.67 ± 0.04	22.0 ± 1.2	22.0
d250	9.3	119.2 ± 2.5	0.63 ± 0.03	8.8 ± 0.5	16.5
d190	7.4	109.4 ± 3.1	0.60 ± 0.04	6.4 ± 0.1	14.1
d130	5.2	88.2 ± 2.7	0.57 ± 0.05	3.2 ± 0.2	10.6
d90	2.9	70.1 ± 1.9	0.53 ± 0.05	1.7 ± 0.5	7.8
d40	1.6	61.7 ± 2.3	0.49 ± 0.06	1.0 ± 0.5	3.2

[a] Different from the previous works,[44,45] the spin−orbit scattering time (length) is no longer a fitting parameter in our theory for Dirac fermions,[27] and ℓ is calculated from the semiclassical conductivity. ℓ_ϕ is fitted from magnetoconductivity curves at 2.1 K. p is fitted from the relation $\ell_\phi \propto T^{-p/2}$ as shown in Figure 3c and d. ε_r is fitted from the slope curves in Figure 4b, and ε_r^{em} is calculated from the Bruggeman effective medium theory (eq 2). d190 means the edge-to-edge distance between two antidots is 190 nm.

known that conventional electrons will be localized at low temperatures in a 2D disordered metal.[19] On the contrary, the surface massless Dirac electrons of a topological insulator are expected to be immune to localization,[40,41] which is evidenced by the WAL-type negative magnetoconductivity in Figure 3. The electron−electron interaction becomes an indispensable ingredient to resolve the puzzle on the coexistence of localization tendency in $\sigma(T)$ and WAL in $\sigma(B)$ in the same sample. A similar localization tendency was also observed in the previous studies of Bi_2Se_3 and Bi_2Te_3 thin films[20−25] and was suggested to be due to the interaction, but convincing quantitative comparison is still lacking.[26] So far only the theory for conventional electrons was exploited for the surface electrons in topological insulators.[17−19]

In the theory for the gapless Dirac fermions of topological surface states,[27] two mechanisms contributing to the ln$T$ dependence of the conductivity are considered: one is the quantum interference, and the other is the interplay of the electron−electron interaction and disorder scattering. For gapless surface fermions of topological insulators, the quantum interference effect gives rise to the WAL effect,[42,43] which exhibits the negative magnetoconductivity as shown in Figure 3a and produces a negative contribution to the slope κ of $\sigma(T)$ curves. A small external magnetic field quickly quenches the quantum interference effect, leading to a rapid increase of the slope κ in Figures 2b and d. After the quantum interference is quenched when $B > 0.5$ T, the saturated slope κ contains only the contribution from the electron−electron interaction named as κ^{ee}. For gapless Dirac fermions of topological insulators,[27]

$$\kappa^{ee} = 1 - \frac{1}{\pi}\frac{\arctan\sqrt{1/x^2 - 1}}{\sqrt{1 - x^2}}, \quad x \equiv \frac{8\pi\varepsilon_0\hbar}{e^2}v\varepsilon_r \quad (1)$$

where $\hbar$ is the reduced Planck constant, e is the electron charge, v is the effective velocity of the surface fermions, and ε_0 and ε_r are the vacuum and relative dielectric constants, respectively. Equation 1 shows

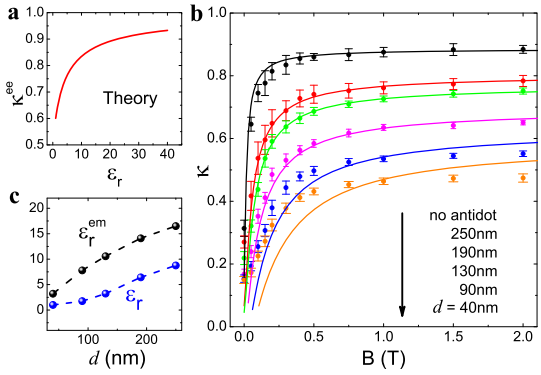

Figure 4. (a) Calculated slope κ^{ee} as a function of relative dielectric constant ε_r for gapless Dirac fermions. $v\hbar$ is chosen to be 2.5 eV·Å, comparable with those in the experiment.[16] (b) Slope κ of conductivity−ln$T$ curve as a function of magnetic field B for different antidot distances d. The measured κ (scatters) are fitted by the theory (solid curves).[27,38] (c) Dielectric constant as a function of d, obtained by fitting the transport theory (ε_r) and calculated from the Bruggeman effective medium theory (ε_r^{em}),[46] respectively. The intrinsic dielectric constant $\varepsilon_b = 22.0$ of the no-antidot sample is extracted by fitting the transport theory.

that κ^{ee} could be changed by modifying either v or ε_r. In comparison with v the relative dielectric constant ε_r is more likely to be changed by inducing an antidot array, because it takes into account the effects of the lattice ions and valence electrons. For fixed v, we have calculated κ^{ee} as a function of ε_r for the surface fermions as plotted in Figure 4a. One can see that κ^{ee} decreases monotonically with decreasing ε_r. A qualitative comparison of Figures 4a and 2c, where the linear slopes of $\sigma(T)$ at $B = 2$ T decrease monotonically as the antidot density increases, implies that one of the effects of antidot array is to reduce the effective dielectric constant of the system and to further modulate the contribution from the electron−electron interaction to the slope κ of $\sigma(T)$. The denser the antidot array, the smaller the relative dielectric constant.

Furthermore, in order to extract ε_r from the experimental data, the measured dependences of slopes κ of ln$T$-dependent conductivity on applied magnetic fields ($0 < B < 2$ T) are plotted in Figure 4b as symbols for all samples. These dependences are fitted using the quantum transport theory of interacting and disordered surface fermions (see solid lines in Figure 4b).[27,38] The ε_r as a fitting parameter are obtained for all samples and are shown in Table 1. It is clear that ε_r monotonically decreases when the density of the antidot array is increased. A notable deviation occurring between the fitting curves and the measured slopes for the samples d90 and d40 may result from the size effect, as the sample becomes a combination of 2D and quasi-1D conducting channels, as their phase coherence lengths at 2.1 K are comparable with their antidot distances d, as shown in Table 1. This limits the applicability of the theory for 2D systems.

We can further compare the fitted ε_r from the transport data with that evaluated from the classical Bruggeman effective medium theory expressed as[46]

$$f_a\frac{\varepsilon_a - \varepsilon_r^{em}}{\varepsilon_a + 2\varepsilon_r^{em}} + f_b\frac{\varepsilon_b - \varepsilon_r^{em}}{\varepsilon_b + 2\varepsilon_r^{em}} = 0 \qquad (2)$$

where f_a and f_b are the volume fraction occupied by the medium a with relative dielectric constant ε_a and medium b with ε_b, respectively, and ε_r^{em} is the effective relative dielectric constant of the heterogeneous mixture of medium a and b. We set $\varepsilon_a = 1$ for antidot vacuum and extract $\varepsilon_b = 22.0$ as the intrinsic dielectric constant of our Bi_2Te_3 thin film by the fitting curve for the no-antidot sample in Figure 4b. The ε_r^{em} values of different samples calculated from eq 2 are shown in Table 1. For comparison, the relative dielectric constants obtained by the two methods are plotted as a function of d in Figure 4c. It is clear that both ε_r and ε_r^{em} show the same tendency when d is varied, although their magnitudes are different. This difference is not surprising, as the classical Bruggeman effective medium theory is just a rough estimate.

The applicability of modulating the effective dielectric constant by an antidot array can be evidenced by the average distance between surface electrons in quantum transport. Considering the surface states as an ideal Dirac cone, the average distance $2\sqrt{\pi}/k_F$ is about several nanometers for the Fermi wave vector $k_F \approx 0.1$ Å^{-1}. However, the quantum conductivity, especially its temperature variation at low temperatures, is contributed by electrons near the Fermi surface, not all electrons in the Fermi sea. The electron density near the Fermi surface can be roughly estimated as the product of the density of states at the Fermi energy and k_BT (k_B is Boltzmann's constant and T is temperature). Therefore, the average distance of surface electrons is estimated to be about 40 to 135 nm from 10 to 1 K.[38] This is comparable with the size and separation of the antidots, and it is reasonable to conclude that the antidot array can change the effective dielectric constant in the film for those electrons contributing to the quantum transport.

CONCLUSIONS

The main observation in this work is that the denser antidots in topological insulator thin films suppress the localization tendency of conduction electrons. The fitting exponent p in the temperature dependence of the phase coherent length indicates the dominant role played by the electron−electron interaction. The phenomena can be viewed as the antidot-array-induced reduction of the effective dielectric constant of the system. These reveal that the widely observed localization tendency in low-temperature conductivity of topological insulators results from the interplay of many-body interaction and disorder scattering. Although the surface electrons are usually considered to be insensitive to scattering by impurities or disorders or not to be localized by disorder,[40,41] our experiments suggest that this should be reexamined when a many-body interaction comes into play.

METHODS

The 20 nm thick Bi_2Te_3 thin film used in the experiment was grown by molecular beam epitaxy on a (111) semi-insulating GaAs substrate with an undoped 85 nm thick ZnSe buffer layer. Standard Hall measurement reveals that the Bi_2Te_3 thin film has an electron carrier concentration and mobility of 1.5×10^{19} cm^{-3} and 310 cm^2 V^{-1} s^{-1}, respectively, at 2.1 K. The Bi_2Te_3 Hall bar with dimensions 60 μm × 15 μm was first fabricated using standard photolithographic processes. Then a series of antidots arranged in a periodic triangular lattice were fabricated between the voltage-measuring probes with electron beam lithography and dry etching techniques. Ohmic contacts of electrodes are formed by evaporation of Cr(5 nm)/Au(100 nm). All transport measurements were conducted in a Quantum Design physical property measurement system with a 14 T superconducting magnet and a base temperature of 2 K. All samples are measured in pulse-delta mode using a Keithley 6221 as the current source and a Keithley 2182A as the voltage meter.

Conflict of Interest: The authors declare no competing financial interest.

Acknowledgment. This work was supported in part by the Research Grants Council of Hong Kong under Grant Nos. 605011, 604910, SEG CUHK06, and 17304414 and in part by the National Natural Science Foundation of China under Grant No. 11204183. The electron-beam lithography facility is supported by the Raith-HKUST Nanotechnology Laboratory at MCPF (SEG HKUST08).

Supporting Information Available: Data fitting, mean free path, threshold temperature, and average distance between electrons near the Fermi surface. This material is available free of charge *via* the Internet at http://pubs.acs.org.

REFERENCES AND NOTES

1. Moore, J. E. The Birth of Topological Insulators. *Nature* **2010**, *464*, 194–198.
2. Hasan, M. Z.; Kane, C. K. Colloquium: Topological Insulators. *Rev. Mod. Phys.* **2010**, *82*, 3045–3067.
3. Qi, X. L.; Zhang, S. C. Topological Insulators and Superconductors. *Rev. Mod. Phys.* **2011**, *83*, 1057.
4. Shen, S. Q. *Topological Insulators*; Springer: Berlin, 2012.
5. Fidkowski, L.; Kitaev, A. The Effects of Interactions on the Topological Classification of Free Fermion Systems. *Phys. Rev. B* **2010**, *81*, 134509.
6. Wang, Z.; Qi, X. L.; Zhang, S. C. Topological Order Parameters for Interacting Topological Insulators. *Phys. Rev. Lett.* **2010**, *105*, 256803.
7. Ostrovsky, P. M.; Gornyi, I. V.; Mirlin, A. D. Interaction-Induced Criticality in Z_2 Topological Insulators. *Phys. Rev. Lett.* **2010**, *105*, 036803.
8. Raghu, S.; Qi, X. L.; Honerkamp, C.; Zhang, S. C. Topological Mott Insulators. *Phys. Rev. Lett.* **2008**, *100*, 156401.
9. Pesin, D.; Balents, L. Mott Physics and Band Topology in Materials with Strong Spin-Orbit Interaction. *Nat. Phys.* **2010**, *6*, 376.
10. Culcer, D. Linear Response Theory of Interacting Topological Insulators. *Phys. Rev. B* **2011**, *84*, 235411.
11. Yu, S. L.; Xie, X. C.; Li, J. X. Mott Physics and Topological Phase Transition in Correlated Dirac Fermions. *Phys. Rev. Lett.* **2011**, *107*, 010401.

12. Zhang, X.; Zhang, H. J.; Wang, J.; Felser, C.; Zhang, S. C. Actinide Topological Insulator Materials with Strong Interaction. *Science* **2012**, *335*, 1464–1466.
13. Das Sarma, S.; Li, Q. Many-Body Effects and Possible Superconductivity in the Two-Dimensional Metallic Surface States of Three-Dimensional Topological Insulators. *Phys. Rev. B* **2013**, *88*, 081404(R).
14. Xia, Y.; Qian, D.; Hsieh, D.; Wray, L.; Pal, A.; Lin, H.; Bansil, A.; Grauer, D.; Hor, Y. S.; Cava, R. J.; *et al*. Observation of a Large-Gap Topological-Insulator Class with a Single Dirac Cone on the Surface. *Nat. Phys.* **2009**, *5*, 398–402.
15. Zhang, H. J.; Liu, C. X.; Qi, X. L.; Dai, X.; Fang, Z.; Zhang, S. C. Topological Insulators in Bi_2Se_3, Bi_2Te_3 and Sb_2Te_3 with a Single Dirac Cone on the Surface. *Nat. Phys.* **2009**, *5*, 438–442.
16. Chen, Y. L.; Analytis, J. G.; Chu, J. H.; Liu, Z. K.; Mo, S. K.; Qi, X. L.; Zhang, H. J.; Lu, D. H.; Dai, X.; Fang, Z.; *et al*. Experimental Realization of a Three-Dimensional Topological Insulator, Bi_2Te_3. *Science* **2009**, *325*, 178–181.
17. Altshuler, B. L.; Aronov, A. G. Zero Bias Anomaly in Tunnel Resistance and Electron-Electron Interaction. *Solid State Commun.* **1979**, *30*, 115.
18. Fukuyama, H. Effects of Interactions on Non-Metallic Behaviors in Two-Dimensional Disordered Systems. *J. Phys. Soc. Jpn.* **1980**, *48*, 2169–2170.
19. Lee, P. A.; Ramakrishnan, T. V. Disordered Electronic Systems. *Rev. Mod. Phys.* **1985**, *57*, 287–337.
20. Wang, J.; DaSilva, A. M.; Chang, C. Z.; He, K.; Jain, J. K.; Samarth, N.; Ma, X. C.; Xue, Q. K.; Chan, M. H. W. Evidence for Electron-Electron Interaction in Topological Insulator Thin Films. *Phys. Rev. B* **2011**, *83*, 245438.
21. Liu, M. H.; Chang, C. Z.; Zhang, Z. C.; Zhang, Y.; Ruan, W.; He, K.; Wang, L. L.; Chen, X.; Jia, J. F.; Zhang, S. C.; *et al*. Electron Interaction-Driven Insulating Ground State in Bi_2Se_3 Topological Insulators in the Two-Dimensional Limit. *Phys. Rev. B* **2011**, *83*, 165440.
22. Chen, J.; He, X. Y.; Wu, K. H.; Ji, Z. Q.; Lu, L.; Shi, J. R.; Smet, J. H.; Li, Y. Q. Tunable Surface Conductivity in Bi_2Se_3 Revealed in Diffusive Electron Transport. *Phys. Rev. B* **2011**, *83*, 241304(R).
23. Takagaki, Y.; Jenichen, B.; Jahn, U.; Ramsteiner, M.; Friedland, K. J. Weak Antilocalization and Electron-Electron Interaction Effects in Cu-Doped Bi_2Se_3 Films. *Phys. Rev. B* **2012**, *85*, 115314.
24. Chiu, S. P.; Lin, J. J. Weak Antilocalization in Topological Insulator Bi_2Te_3 Microflakes. *Phys. Rev. B* **2013**, *87*, 035122.
25. Roy, A.; Guchhait, S.; Sonde, S.; Dey, R.; Pramanik, T.; Rai, A.; Movva, H. C. P.; Colombo, L.; Banerjee, S. K. Two-Dimensional Weak Anti-localization in Bi_2Te_3 Thin Film Grown on Si(111)-(7×7) Surface by Molecular Beam Epitaxy. *Appl. Phys. Lett.* **2013**, *102*, 163118.
26. Bardarson, J. H.; Moore, J. E. Quantum Interference and Aharonov−Bohm Oscillations in Topological Insulators. *Rep. Prog. Phys.* **2013**, *76*, 056501.
27. Lu, H. Z.; Shen, S. Q. Finite-Temperature Conductivity and Magnetoconductivity of Topological Insulators. *Phys. Rev. Lett.* **2014**, *112*, 146601.
28. Checkelsky, J. G.; Hor, Y. S.; Liu, M. H.; Qu, D. X.; Cava, R. J.; Ong, N. P. Quantum Interference in Macroscopic Crystals of Nonmetallic Bi_2Se_3. *Phys. Rev. Lett.* **2009**, *103*, 246601.
29. Peng, H. L.; Lai, K. J.; Kong, D. S.; Meister, S.; Chen, Y. L.; Qi, X. L.; Zhang, S. C.; Shen, Z. X.; Cui, Y. Aharonov-Bohm Interference in Topological Insulator Nanoribbons. *Nat. Mater.* **2010**, *9*, 225.
30. Chen, J.; Qin, H. J.; Yang, F.; Liu, J.; Guan, T.; Qu, F. M.; Zhang, G. H.; Shi, J. R.; Xie, X. C.; Yang, C. L.; *et al*. Gate-Voltage Control of Chemical Potential and Weak Antilocalization in Bi_2Se_3. *Phys. Rev. Lett.* **2010**, *105*, 176602.
31. He, H. T.; Wang, G.; Zhang, T.; Sou, I. K.; Wang, G. K. L.; Wang, J. N.; Lu, H. Z.; Shen, S. Q.; Zhang, F. C. Impurity Effect on Weak Antilocalization in the Topological Insulator Bi_2Te_3. *Phys. Rev. Lett.* **2011**, *106*, 166805.
32. Hikami, S.; Larkin, A. I.; Nagaoka, Y. Spin-Orbit Interaction and Magnetoresistance in the Two Dimensional Random System. *Prog. Theor. Phys.* **1980**, *63*, 707.
33. Lu, H. Z.; Shi, J.; Shen, S. Q. Competition between Weak Localization and Antilocalization in Topological Surface States. *Phys. Rev. Lett.* **2011**, *107*, 076801.
34. Lang, M. R.; He, L.; Xiu, F. X.; Yu, X. X.; Tang, J. S.; Wang, Y.; Kou, X. F.; Jiang, W. J.; Fedorov, A. V.; Wang, K. L. Revelation of Topological Surface States in Bi_2Se_3 Thin Films by *in Situ* Al Passivation. *ACS Nano* **2012**, *6*, 295–302.
35. Cha, J. J.; Kong, D. S.; Hong, S. S.; Analytis, J. G.; Lai, K. J.; Cui, Y. Weak Antilocalization in $Bi_2(Se_xTe_{1-x})_3$ Nanoribbons and Nanoplates. *Nano Lett.* **2012**, *12*, 1107–1111.
36. Wang, Z. H.; Qiu, R. L. J.; Lee, C. H.; Zhang, Z. D.; Gao, X. P. A. Ambipolar Surface Conduction in Ternary Topological Insulator $Bi_2(Te_{1-x}Se_x)_3$ Nanoribbons. *ACS Nano* **2013**, *7*, 2126–2131.
37. Gehring, P.; Benia, H. M.; Weng, Y.; Dinnebier, R.; Ast, C. R.; Burghard, M.; Kern, K. A Natural Topological Insulator. *Nano Lett.* **2013**, *13*, 1179–1184.
38. See Supporting Information.
39. Thouless, D. J. Maximum Metallic Resistance in Thin Wires. *Phys. Rev. Lett.* **1977**, *39*, 1167.
40. Bardarson, J. H.; Tworzydlo, J.; Brouwer, P. W.; Beenakker, C. W. J. One-Parameter Scaling at the Dirac Point in Graphene. *Phys. Rev. Lett.* **2007**, *99*, 106801.
41. Nomura, K.; Koshino, M.; Ryu, S. Topological Delocalization of Two-Dimensional Massless Dirac Fermions. *Phys. Rev. Lett.* **2007**, *99*, 146806.
42. Suzuura, H.; Ando, T. Crossover from Symplectic to Orthogonal Class in a Two-Dimensional Honeycomb Lattice. *Phys. Rev. Lett.* **2002**, *89*, 266603.
43. McCann, E.; Kechedzhi, K.; Fal'ko, V. I.; Suzuura, H.; Ando, T.; Altshuler, B. L. Weak-Localization Magnetoresistance and Valley Symmetry in Graphene. *Phys. Rev. Lett.* **2006**, *97*, 146805.
44. Zhang, S. X.; McDonald, R. D.; Shekhter, A.; Bi, Z. X.; Li, Y.; Jia, Q. X.; Picraux, S. T. Magneto-Resistance up to 60 T in Topological Insulator Bi_2Te_3 Thin Films. *Appl. Phys. Lett.* **2012**, *101*, 202403.
45. Dey, R.; Pramanik, T.; Roy, A.; Rai, A.; Guchhait, S.; Sonde, S.; Movva, H. C.P.; Colombo, L.; Register, L. F.; Banerjee, S. K. Strong Spin-Orbit Coupling and Zeeman Spin Splitting in Angle Dependent Magnetoresistance of Bi_2Te_3. *Appl. Phys. Lett.* **2014**, *104*, 223111.
46. Aspnes, D. E. Local-Field Effects and Effective-Medium Theory: A Microscopic Perspective. *Am. J. Phys.* **1982**, *50*, 704.